

Facile Method for Preparation of Porous Carbon Derived from Biomass for High Performance Supercapacitors

Yao Lu, Fen Xu*, Lixian Sun*, Yi Wu, Yongpeng xia, Xinran Cai, Ningkuan Zhong, Huanzhi Zhang, Bin Li, Hailiang Chu

Guangxi Key Laboratory of Information Materials, Guangxi Collaborative Innovation Center of Structure and Property for New Energy and Materials, School of Material Science and Engineering, Guilin University of Electronic Technology, Guilin, 541004, P. R. China

*E-mail: xufen@guet.edu.cn, sunlx@guet.edu.cn

Received: 2 July 2019 / Accepted: 17 September 2019 / Published: 29 October 2019

A facile method is adopted to obtain three-dimensional porous carbonaceous material from biomass (fish seed) by pyrolysis and activation. The three-dimensional porous carbonaceous material is then fabricated as electrodes for a supercapacitor. Owing to fish seed being rich in elemental oxygen and nitrogen, the heteroatoms can introduce a pseudo-capacitance without doping. Scanning electron microscopy (SEM) analysis results show that the three-dimensional porous carbonaceous material exhibits an interconnected porous structure, which consists of micropores, mesopores and macropores. Adsorption-desorption measurements determine that its surface area is $3232 \text{ m}^2 \cdot \text{g}^{-1}$. Electrochemical measurements show that the biomass-derived porous carbon material displays a relatively high specific capacitance of $350 \text{ F} \cdot \text{g}^{-1}$ at $0.5 \text{ A} \cdot \text{g}^{-1}$ and an initial capacitance retention of 90.9% after 10,000 cycles in a three-electrode system, where KOH (6 M) is used as the electrolyte. In addition, the porous carbon material is also tested in a two-electrode system and exhibits a specific capacitance of $250 \text{ F} \cdot \text{g}^{-1}$ at $1 \text{ A} \cdot \text{g}^{-1}$, and the specific capacitance retention reaches 94% after 10,000 cycles at $10 \text{ A} \cdot \text{g}^{-1}$. Furthermore, the energy density of the supercapacitor is approximately $8.68 \text{ Wh} \cdot \text{kg}^{-1}$ at a power density of $125 \text{ W} \cdot \text{kg}^{-1}$ in the two-electrode system.

Keywords: Biomass; Direct pyrolysis; Porous carbon; Supercapacitors

1. INTRODUCTION

Owing to economic development along with the excessive use of fossil energy resources, a solution to environmental problems, such as air pollution, is urgently being sought [1-3]. Based on this, the study of electrochemical energy storage devices has been attracting increasing attention. A supercapacitor is a common energy storage device, which can operate at a much higher power density than a battery and exhibit a higher energy density than a conventional dielectric capacitor [4-6]. Because

of the high power density [7], long cycle life [8] and rapid charge-discharge rate [9], the supercapacitor is considered as a promising energy storage device. Great progresses in theoretical research and practical application of supercapacitors have been made, but the problems of insufficient energy density and high cost still remain [10-12]. Electrode materials, as the core component, play an important role in a supercapacitor. Supercapacitor materials can be classified into carbon materials [13, 14], metal oxides [15, 16] and conductive polymers [17, 18]. Activated carbon (AC), owing to its high specific surface area, good electronic conductivity and excellent chemical stability, is regarded as the most widely adopted electrode material [19-21]. As a source of activated carbon materials, biomass possesses many advantages, because it is bountiful, renewable, non-toxic and low cost. Therefore, biomass has played an important role in the preparation of functional carbon materials. At the same time, biomass usually possesses a variety of elements, which could introduce pseudo-capacitance to improve the electrochemical properties of the functional carbon materials [22-24].

Fish seed, as a renewable and familiar biomass, is very common in daily life. Fish seed contains many proteins and minerals, such as calcium, phosphorus and iron, as well as large amounts of brain phospholipids. The heteroatoms can be introduced to the carbon materials obtained from fish seed and effectively enhance the electrochemical performance of the electrode material without extra doping. Therefore, fish seed is selected as the carbon source in this work. The electrochemical performances of the carbon materials obtained from fish seed are studied. The experimental results indicate that a three-dimensional porous carbonaceous material is obtained from fish seed, and the porous carbon reveals a good electrochemical property for use in a supercapacitor.

2. EXPERIMENTAL

2.1. Materials synthesis

A typical synthesis method was adopted, where the fish seed was first washed by distilled water and dried in an air-blast drying box at 85 °C for 48 h. Then, the dried fish seed was broken into small pieces and calcined in a tube furnace at 500 °C for 2 h protected by a nitrogen atmosphere. The carbon precursor and potassium hydroxide were mixed at a mass ratio of 1.0:(1.0~4.0) and the activation process was conducted in a tube furnace at 800 °C for 2 h protected under a nitrogen atmosphere. The product was soaked with a 1 M HCl solution and filtered with distilled water until the filtrate was neutral. The precipitate was finally dried and ground to obtain the fish-seed-based multi-hole carbon material. The samples were named as YZ 800(1-1), YZ 800(1-2), YZ 800(1-3) and YZ 800(1-4), respectively.

2.2. Materials characterizations

The morphology and microstructure of the samples were examined by scanning electron microscopy (SEM, Quanta 200, FEI, USA) and transmission electron microscopy (JEM2010, JEOL, Japan). The crystallographic structure was determined by X-ray diffraction (XRD, Bruker-D8 Advance diffractometer, Germany). Raman spectra were recorded using a LabRAM HR Evolution spectrometer

(Horiba JY, France). The nitrogen adsorption-desorption measurements were conducted using a Quantachrome sorptometer Autosorb iQ2 (USA) at $-196\text{ }^{\circ}\text{C}$. The surface element analysis was performed by means of X-ray photoelectron spectroscopy (XPS, Thermo Scientific Escalab 250Xi, USA).

2.3. Electrochemical measurements

The electrode materials were first tested in a three-electrode system using an aqueous KOH (6 M) solution as an electrolyte. Each electrode sample was made up of 80 wt% carbon material, 10 wt% acetylene black and 10 wt% polytetrafluoroethylene (PTFE) binder, which were mixed in ethanol and painted onto the nickel foam ($1\times 1\text{ cm}^2$) under $80\text{ }^{\circ}\text{C}$ for 12 h. The loading weight density for each nickel foam was approximately 10 mg cm^{-2} . A Pt foil was used as the counter electrode and Hg/HgO was the reference electrode. Electrochemical impedance spectroscopy (EIS) and cyclic voltammetry (CV) were conducted using a CHI660e electrochemical workstation (Chenhua Instrument Inc.) and the galvanostatic charge-discharge tests (GCD) were performed using a LAND CT2001A instrument. The parameters of CV, EIS and GCD were set as -1 to 0 V , 0.1 - 100 kHz with a perturbation amplitude of 5 mV and -1 to 0 V , respectively. Moreover, the symmetric supercapacitor was built using the same two electrode materials and tested in the voltage window of 0 - 1 V .

3. RESULTS AND DISCUSSION

3.1. Morphological and structural characterization

The morphology of the samples of YZ-800 (namely, YZ 800(1-1), YZ 800(1-2), YZ 800(1-3) and YZ 800(1-4)) were characterized by SEM (see Fig. 1)). As we can see from the images (Fig. 1(a)-(d)), after being activated, the surface of the activated carbon was etched by many pores with different pore sizes. With the increase of KOH activation, the pore size became larger, and when the activation ratio was 1:4, the surface pore structure collapsed. Among them, the YZ 800(1-3) showed an excellent pore structure, which is beneficial to accelerate the entry of electrolyte ions into the pores to improve the energy storage performance. The microstructure information of YZ 800(1-3) was further provided by TEM. Fig. 2(a) and (b) indicates that the sample YZ 800(1-3) possessed a layered structure with abundant micropores, so YZ 800(1-3) was a defective microporous and amorphous compound with structural disorder. The EDX element mappings (Fig. 2(c)-(j)) showed that YZ 800(1-3) contained carbon, nitrogen and oxygen, and trace elements such as sulfur, phosphorus, iron and calcium.

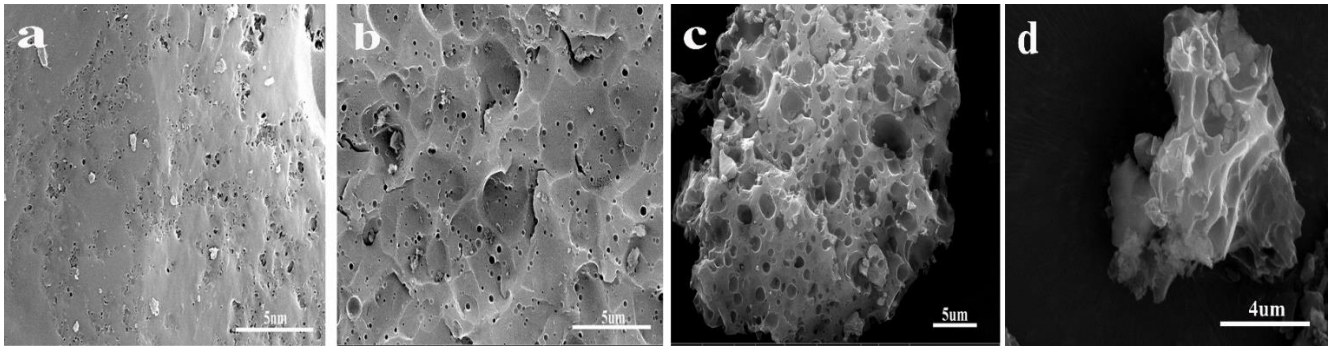


Figure 1. SEM image of YZ 800, (a): YZ 800(1-1); (b): YZ 800(1-2); (c): YZ 800(1-3); (d): YZ 800(1-4).

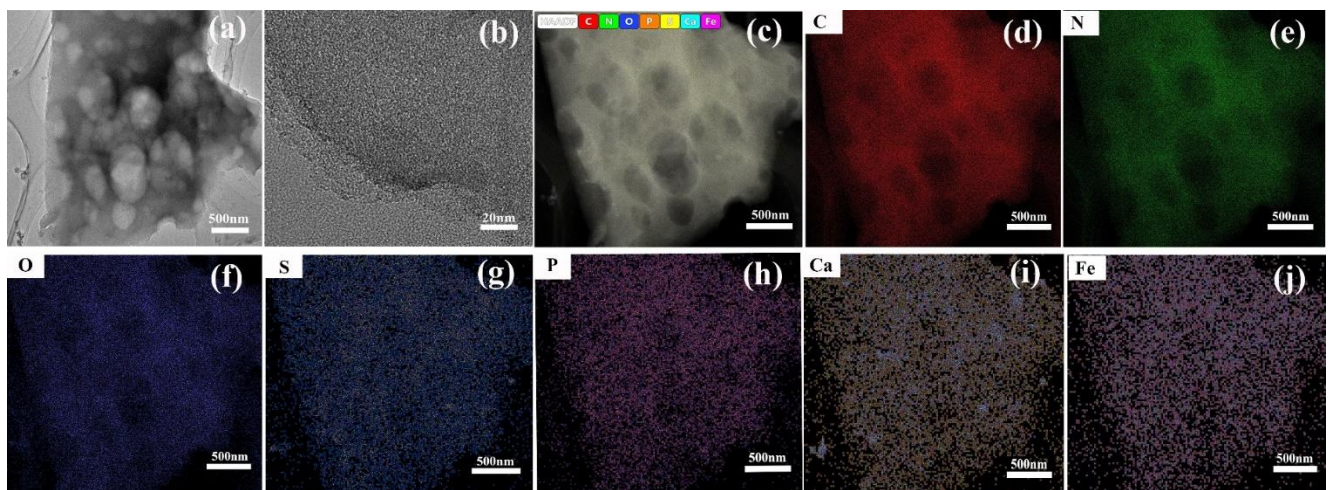


Figure 2. TEM image of YZ 800, (a): YZ 800(1-3); (b): HRTEM image of YZ 800(1-3); (c-j): EDX elemental mapping images of YZ 800(1-3).

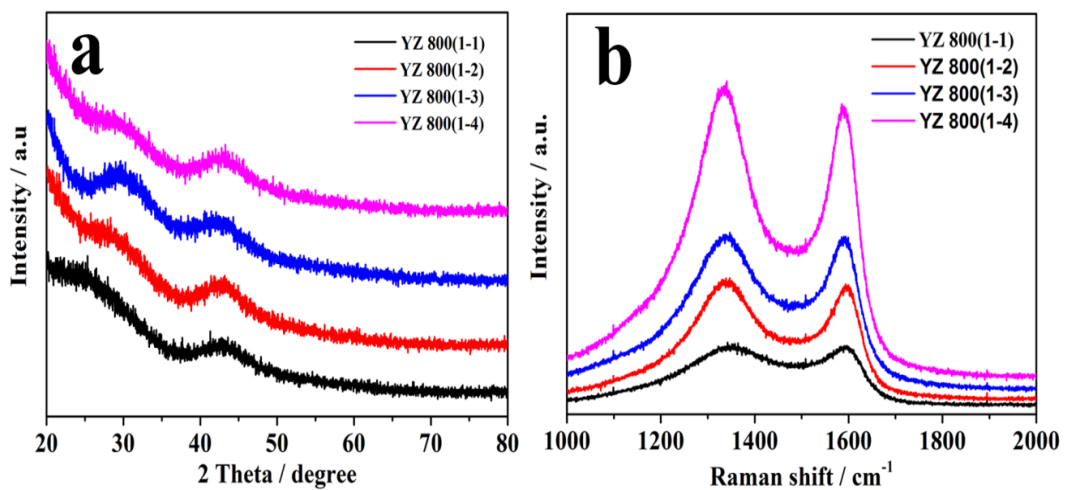


Figure 3. XRD patterns (a) and Raman spectra (b) of YZ 800.

The structures of YZ 800 were determined by XRD and Raman spectroscopy. From the XRD spectra (see Fig. 3(a)), two broad diffraction peaks, which corresponded to the (002) and (100) crystal planes of the graphite structure, respectively, indicated the amorphous nature and disordered graphitic-type carbon [14, 25]. Fig. 3(b) shows the Raman spectra of the activated porous carbon materials. There were two characteristic peaks in the Raman spectra at the wavelengths 1335 cm^{-1} and 1585 cm^{-1} , which corresponded to the D and G peaks of graphite, respectively. The D peak was a defect peak caused by low symmetry or irregularity of the carbon materials, and was related to a miscellaneous, defect, swing bond in the graphite structure [26], and the G peak represented the graphite peak, which reflected the degree of graphitization, and was caused by the sp^2 vibration of the hexagonal structure of graphite. The intensity ratio of I_D/I_G indicates the level of graphitic ordering, where a relatively lower ratio usually demonstrates an inferior graphitization. The activation process can result in producing nanopores and defects in the precursor. With an increase of KOH activation, the ratio of the integral intensities gradually decreases. The obtained results show that the I_D/I_G values were 0.98, 1.03, 1.04 and 1.07 for YZ 800(1-1), YZ 800(1-2), YZ 800(1-3) and YZ 800(1-4), respectively. The increased defects can be used as active and adsorption sites so as to improve the performance and catalytic activity of supercapacitors [27].

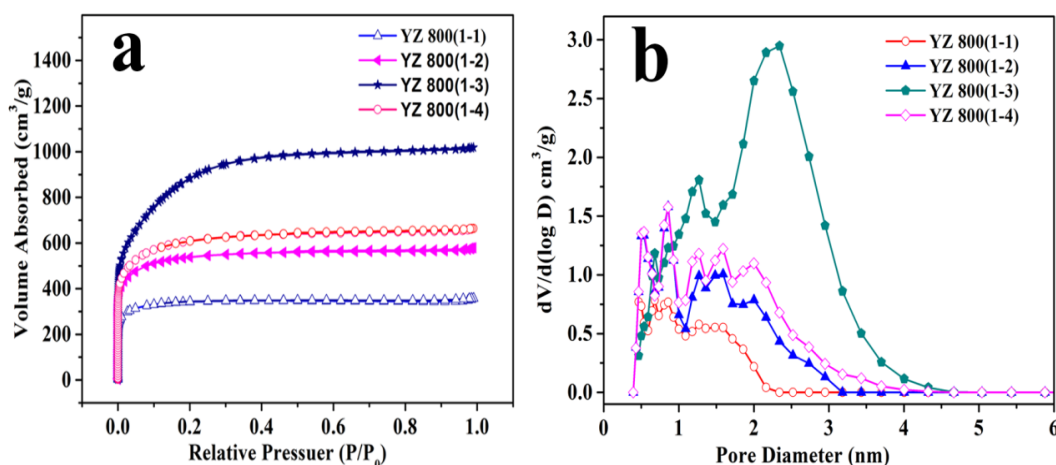


Figure 4. (a): Nitrogen adsorption isotherms of YZ 800; (b): pore size distribution curves of YZ 800.

Table 1. Structure parameters of YZ 800

Samples	BET SSA ($\text{m}^2 \cdot \text{g}^{-1}$)			Pore volume ($\text{cm}^3 \cdot \text{g}^{-1}$)			Pore size (nm)
	Total	Micro	External	Total	Micro	External	
YZ 800(1-1)	1143	1076	67	0.55	0.50	0.05	1.93
YZ 800(1-2)	1735	1495	240	0.89	0.72	0.17	2.06
YZ 800(1-3)	3232	1961	1271	1.57	0.80	0.77	1.95
YZ 800(1-4)	2007	1591	416	1.03	0.76	0.27	2.05

To explore the porous structure, the N_2 adsorption-desorption isotherms were examined. As we can see from the adsorption-desorption isotherms (shown in Fig. 4(a)), all the samples showed Type-I adsorption isotherm characteristics, and the volumetric adsorptions increased sharply when the relative pressure P/P_0 was low, which indicated the sample contained plenty of micropores. The pore structure parameters of YZ 800 are listed in Table 1. The specific BET surface areas of YZ 800(1-1), YZ 800(1-2), YZ 800(1-3) and YZ 800(1-4) respectively were 1143, 1735, 3232 and 2007 $m^2 g^{-1}$, which corresponded to their pore volumes of 0.55, 0.89, 1.57 and 1.03 $cm^3 g^{-1}$. When the activation mass ratio was increased to 1:3, the specific surface area and the pore volume of YZ 800(1-3) reached a maximum. In addition, all the YZ 800 compounds possessed a hierarchical pore structure with observable pore sizes ranging from 0.5 to 5 nm, and the sample YZ 800(1-3) exhibited two peaks of micropores at 0.7 and 1.5 nm, and the mesopores had a maximal peak at 2.4 nm. The existence of different nano-scale holes yielded a typical three-dimensional hierarchical porous structure. The high BET surface area not only ensures a highly contactable surface area, but also provides a channel for the migration of electrolyte ions, and encourages the sample to adsorb more electrolyte ions, which will lead to further high electrical double-layer capacitors (EDLC) [26, 28, 29].

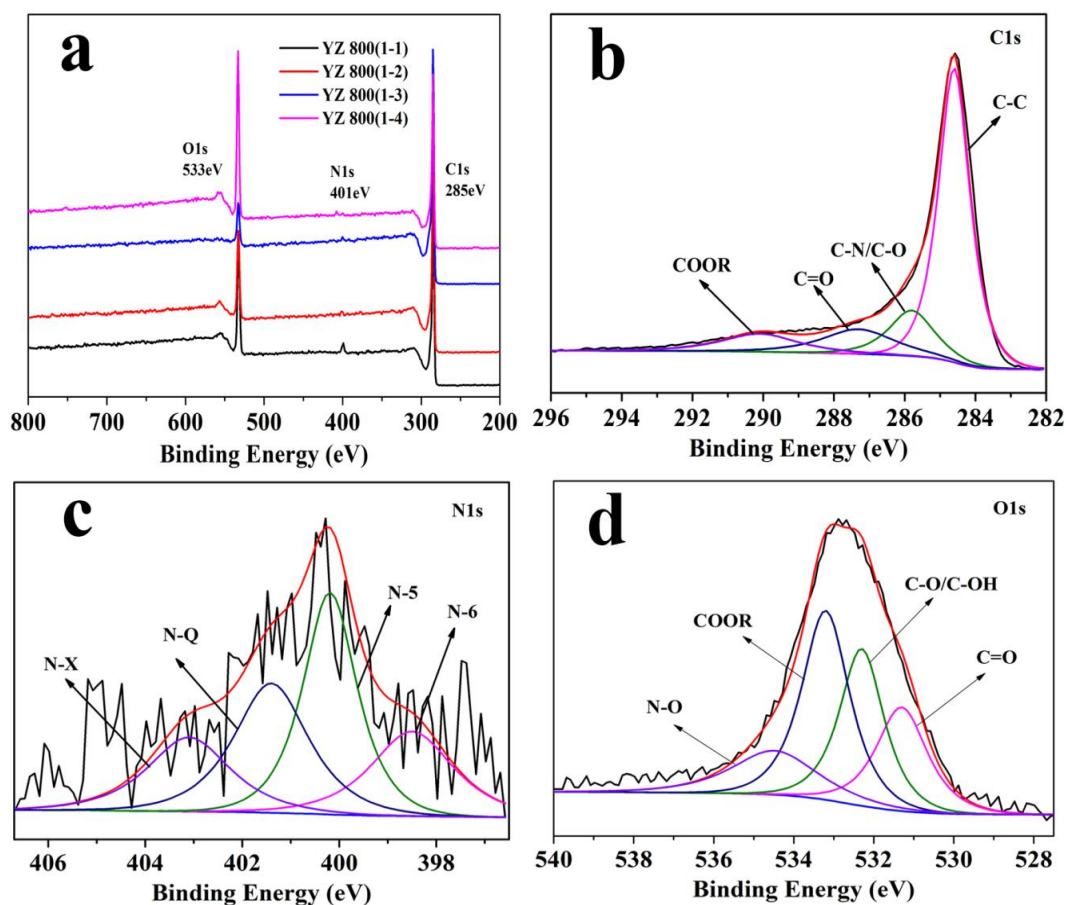


Figure 5. (a): XPS spectra of YZ 800; (b): C1s peak differentiation fitting spectra of YZ 800(1-3); (c): N1s peak differentiation fitting spectra of YZ 800(1-3); (d): O1s peak differentiation fitting spectra of YZ 800(1-3).

Table 2. Surface element composition tested by XPS

Samples	Elemental content (wt%)		
	C	N	O
YZ 800(1-1)	76	4	20
YZ 800(1-2)	83.75	1.75	14.5
YZ 800(1-3)	90.1	1.5	8.4
YZ 800(1-4)	72.02	2.58	25.4

The surface compositions of YZ 800 were subsequently measured. Owing to the amount of sulfur, phosphorus, iron and calcium elements being small, only carbon, nitrogen and oxygen elements were analyzed. As we can see from Fig. 5(a), all the XPS survey spectra showed three peaks, two strong peaks were related to C1s and O1s with binding energies of 285 and 532 eV, and the binding energy of N1s corresponded to a weak peak at 401 eV. Table 2 lists the content of elemental C, N and O in YZ 800. When the ratio of KOH was increased from 1:1 to 1:3, the element content of N decreased from 4% to 1.5%, and the content of O decreased from 20% to 8.4%. The fine analyses of the C1s, N1s and O1s spectra for the YZ 800(1-3) sample were performed using the peak differentiation fitting method. The C1s spectrum, shown in Fig. 5(b), was deconvoluted into four peaks, which corresponded to the C-C (284.6 eV), C-N/C-O (285.8 eV), C=O(287.3eV) and COOR (290 eV) groups, respectively. The N1s spectrum could be matched by four peaks at 398.5, 400.2, 401.4 and 403 eV, which corresponded to pyridinic (N-6), pyrrolic and/or pyridinic (N-5), quaternary nitrogen (N-Q) and oxidized nitrogen (N-X) [30], respectively. The presence of pyridinic nitrogen is beneficial to the wettability among electrodes and electrolytes and improves the electron distribution of electrodes. Moreover, the quaternary nitrogen is good for the conductivity of the carbon electrodes, all of which can enhance the capacitive performance [31]. The deconvolution of the O1s peak displayed three peaks at 531.3, 532.3, 533.2 and 534.4 eV, which represented the oxygen atoms in the C=O, C-O/C-OH, COOR and N-O groups. It is known that these groups can provide redox activity to introduce Faradaic pseudocapacitance [32].

3.2. Electrochemical properties

The electrochemical performance of the electrode material was first evaluated by a three-electrode system. Fig. 6(a) shows the cyclic voltammetry (CV) plots of the different carbon materials (YZ 800(1-1), YZ 800(1-2), YZ 800(1-3) and YZ 800(1-4)) at a sweep rate of $50 \text{ mV} \cdot \text{s}^{-1}$. From Fig. 6(a), all the CV curves presented a roughly rectangular shape and had obvious humps, which suggested their combined EDLC and pseudo-capacitance was in response to the redox reactions resulting from the N/O-containing functional groups. Apparently, the YZ 800(1-3) sample exhibited the largest encircled area of the CV curve of the four samples, which was attributed to the largest specific surface, the appropriate pore size and the certain degree of nitrogen and oxygen contents of YZ 800(1-3).

Furthermore, the CV curves ($5\text{--}200\text{ mV}\cdot\text{s}^{-1}$) of YZ 800(1-3) at different scanning rates are shown in Fig. 6(b). The sample maintained a quasi-rectangular shape under the scan rates from 5 to $50\text{ mV}\cdot\text{s}^{-1}$, which indicated that the sample exhibited typical double-layer supercapacitance characteristics of porous carbon in an aqueous electrolyte.

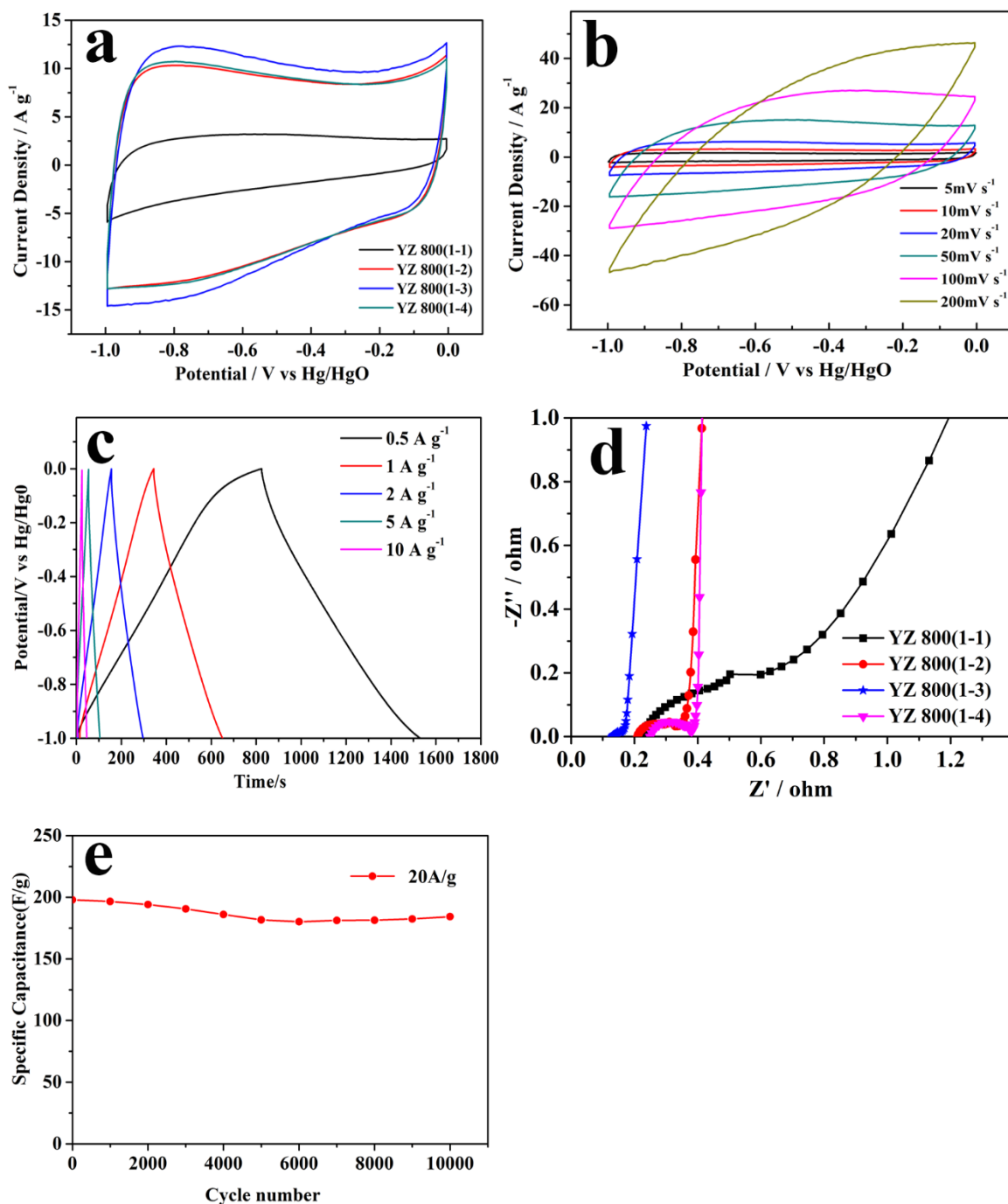


Figure 6. (a): CV curves of as-prepared samples at a scan rate of $50\text{ mV}\cdot\text{s}^{-1}$; (b): CV curves of YZ 800(1-3) at different scan rates; (c): GCD curves of YZ 800(1-3) at different current densities; (d): Nyquist plots of YZ 800; (e): Cycling performance of YZ 800(1-3).

Moreover, it also possessed excellent charge-discharge reversibility. However, the CV curves of the activated carbon electrode began to deviate from the standard rectangular shape when the scan rate was increased to $100 \text{ mV} \cdot \text{s}^{-1}$, and redox peaks could be observed.

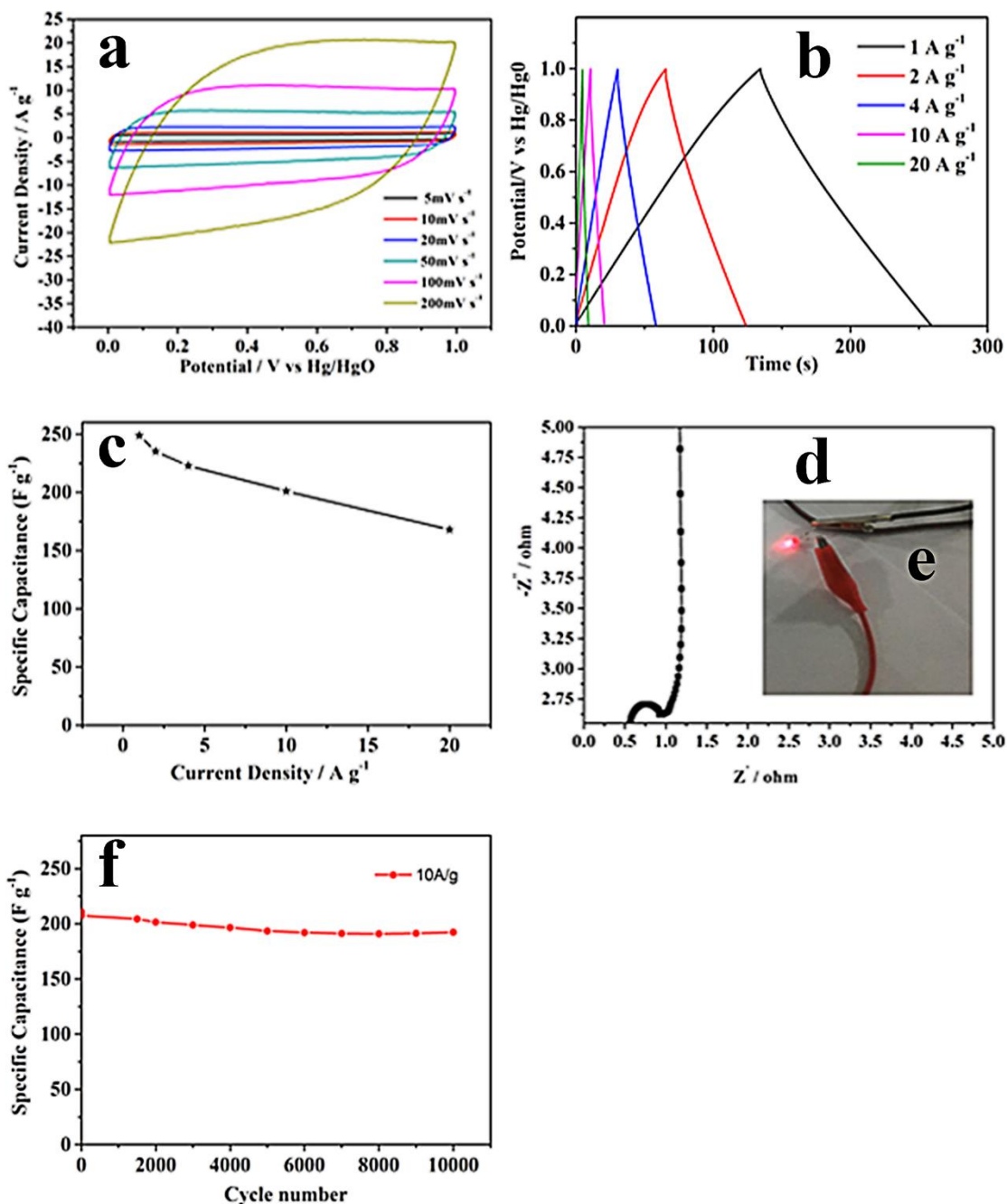


Figure 7. Electrochemical performances of YZ 800(1-3) in a two-electrode system. a) CV curves at various scan rates of 5–200 $\text{mV} \cdot \text{s}^{-1}$; b) GCD curves tested at 0.5–20 $\text{A} \cdot \text{g}^{-1}$; c) specific capacitance at different current densities; d) Nyquist plots; e) LED lit up by a device of two supercapacitors connected in series; f) capacitance retention over 10,000 cycles.

The reason for this may be that the activated carbon material contained impurity atoms, such as O and N, the presence of which, on the surface of carbon materials, may introduce pseudocapacitance

owing to redox reactions [26, 33, 34], and this also agreed with previous tests. Figure 6(c) shows that the GCD curves of electrode materials were increased from 0.5 to 10 $\text{A}\cdot\text{g}^{-1}$. The resulting charge-discharge curves all showed a roughly isosceles triangle shape with no obvious potential drop, which indicated an ideal capacitive behavior and small internal resistance of the prepared sample. The specific capacitances were calculated to be 350, 306, 278, 255 and 213 $\text{F}\cdot\text{g}^{-1}$, which corresponded to the current densities of 0.5, 1, 2, 5, 10 $\text{A}\cdot\text{g}^{-1}$. Furthermore, the EIS of the electrode material was measured to determine the electrochemical mechanism of the material. As shown in Fig. 6 (d), the sample YZ 800(1-3) showed the smallest R_{ct} and R_s values, and the linear curve in the low-frequency region was almost vertical, which indicated a small charge transfer resistance of the material and efficient diffusion of the electrolyte ions. This corresponded to the previously determined excellent electrochemical performance [35-37]. The cycling stability of YZ 800(1-3) was measured using a current density of 20 $\text{A}\cdot\text{g}^{-1}$ (see Fig. 6 (e)). The specific capacitance retention rate was still 90.9% after 10,000 cycles (the capacitance was maintained at 180 $\text{F}\cdot\text{g}^{-1}$), which meant that the material was highly reversible in repeated charge-discharge cycles. This could arise from the multifunctional pore structure and structural stability in the material. The mesopore and macropore structures in the sample facilitated the transfer of the electrolyte, which could alleviate the excessive accumulation of the electrolyte in the micropores and reduce the volume change. In addition, the structural stability and chemical inertness of the porous carbon material also contributed to the negligible structural damage during the charge-discharge cycles [38-40].

Table 3. Specific capacitances of various biomass-based activated carbons

Material	S_{BET} ($\text{m}^2\cdot\text{g}^{-1}$)	Specific capacitance ($\text{F}\cdot\text{g}^{-1}$)	Current density ($\text{A}\cdot\text{g}^{-1}$)	Electrolyte	Ref.
Cotton	2436	283	1	6 M KOH	5
Cornstalk	1588	407	1	1 M H_2SO_4	8
Human hair	2062	340	1	6 M KOH	25
Sakura	1433.8	265.8	0.2	6 M KOH	27
Willow catkin	1533	298	0.5	6 M KOH	28
Tamarinds	846	287	1	1 M KOH	29
Perilla	655	270	0.5	6 M KOH	30
Algae microspheres,	1337.9	353	1	2 M KOH	31
Fish seed	3232	350	0.5	6 M KOH	This work

Next, to investigate the practical application of the YZ 800(1-3) sample, the same mass of the electrodes was constructed into a symmetric supercapacitor and tested in a two-electrode configuration. The electrode material also showed an excellent electrochemistry performance. Figure 7(a) shows that all the CV curves ($5\text{--}200 \text{ mV}\cdot\text{s}^{-1}$) presented quasi-rectangular shapes, which suggested a good EDLC behavior and great reversibility [41]. The GCD curves, as presented in the inset in Fig. 7(b), showed that all the curves exhibited isosceles triangle shapes, which implied an excellent charge-discharge

performance. The calculated specific capacitance is further shown in Fig. 7(c). The specific capacitances were 250, 236, 225, 202 and 192 F g⁻¹ at 1, 2, 4, 10 and 20 A·g⁻¹, respectively (the retention of the specific capacitance still reached 76.8% at 20 A·g⁻¹), where a relatively small degradation was achieved and a remarkable rate performance was demonstrated. Moreover, the Nyquist plot (Fig. 7(d)) exhibited a vertical linear line in the low frequency region, and the R_{ct} and R_s values were 0.4 and 0.6 Ω, respectively. Furthermore, to verify the energy storage application of the electrode material, a device with two supercapacitors in series was assembled. After charging for only 10 seconds, the device could drive an LED bulb to light for 10 minutes, which presented the prospect for practical application, as shown in Fig. 7(e). The energy and power density of the device were also calculated, where the energy density was 8.68 Wh·kg⁻¹ and the power density was 124.9 W·kg⁻¹. In addition, the cycling stability under the galvanostatic charge-discharge was studied (see Fig. 7(f)). The capacitance retention rate of the device was 94% at a current density of 10 A·g⁻¹ after 10,000 cycles, which showed excellent cyclic durability.

4. CONCLUSION

A biomass porous carbonaceous material was successfully prepared from fish seed, which possesses a three-dimensional porous structure, large specific surface area, suitable pore size distribution and excellent electrochemical properties. According to the BET and DFT methods, the prepared sample YZ 800(1-3) exhibited a very high specific surface area of 3232 m²·g⁻¹, a large pore volume of 1.57 cm³·g⁻¹ and the average pore diameter was 1.95 nm. The supercapacitor made from YZ 800(1-3) exhibited a high specific capacitance of 350 F·g⁻¹ at 0.5 A·g⁻¹ and excellent cycling stability (only 9.1% loss of the initial capacitance after 10,000 cycles at 20 A·g⁻¹). Furthermore, the assembled symmetric YZ 800(1-3) supercapacitor exhibited an excellent specific capacitance of 250 F·g⁻¹ at 1 A·g⁻¹ and an impressive long-term cycling stability in a two-electrode system, where its capacitance retention was approximately 94% after 10,000 cycles at 10 A·g⁻¹. It also achieved a high energy density of approximately 8.68 Wh·kg⁻¹ at a power density of 124.9 W·kg⁻¹. All these results suggest that this work provides a new source of biomass for porous carbon material.

ACKNOWLEDGEMENTS

This work was supported by the National Natural Science Foundation of China (U1501242 and 51671062), the Guangxi Collaborative Innovation Centre of Structure and Property for New Energy and Material (2012GXNSFGA06002), Guangxi Science and Technology Project (AD17195073), Guangxi Major Science and Technology Special Project (AA17202030-1) and the Guangxi Key Laboratory of Information Laboratory Foundation (161002-Z, 161002-K and 161003-K).

References

1. P. Chen, L.-K. Wang, G. Wang, M.-R. Gao, J. Ge, W.-J. Yuan, Y.-H. Shen, A.-J. Xie and S.-H. Yu, *Energy Environ. Sci.* 7 (2014) 4095.

2. S. Dutta, A. Bhaumik and K. C. W. Wu, *Energy Environ. Sci.*, 7 (2014) 3574.
3. J. Hou, C. Cao, F. Idrees and X. Ma, *ACS Nano*, 9 (2015) 2556.
4. Y. Chang, G. Zhang, B. Han, H. Li, C. Hu, Y. Pang, Z. Chang and X. Sun, *ACS Appl. Mater. Interfaces*, 9 (2017) 29753.
5. P. Cheng, T. Li, H. Yu, L. Zhi, Z. Liu and Z. Lei, *J. Phys. Chem. C*, 120 (2016) 2079.
6. Z. Li, Z. Xu, X. Tan, H. Wang, C. M. B. Holt, T. Stephenson, B. C. Olsen and D. Mitlin, *Energy Environ. Sci.*, 6 (2013) 871.
7. L. Xie, G. Sun, F. Su, X. Guo, Q. Kong, X. Li, X. Huang, L. Wan, W. Song, K. Li, C. Lv and C.-M. Chen, *J. Mat. Chem. A*, 4 (2016) 1637.
8. C. Wang, D. Wu, H. Wang, Z. Gao, F. Xu and K. Jiang, *J. Mat. Chem. A*, 6 (2018) 1244.
9. D. Saha, Y. Li, Z. Bi, J. Chen, J. K. Keum, D. K. Hensley, H. A. Grappe, H. M. Meyer, III, S. Dai, M. P. Paranthaman and A. K. Naskar, *Langmuir*, 30 (2014) 900.
10. Z. Li, L. Zhang, B. S. Amirkhiz, X. Tan, Z. Xu, H. Wang, B. C. Olsen, C. M. B. Holt and D. Mitlin, *Adv. Energy Mat.* 2 (2012) 431.
11. L. Sun, C. Tian, M. Li, X. Meng, L. Wang, R. Wang, J. Yin and H. Fu, *J. Mat. Chem. A*, 1 (2013) 6462.
12. H. Wang, Z. Xu, A. Kohandehghan, Z. Li, K. Cui, X. Tan, T. J. Stephenson, C. K. King'odu, C. M. B. Holt, B. C. Olsen, J. K. Tak, D. Harfield, A. O. Anyia and D. Mitlin, *Acs Nano*, 7 (2013) 5131.
13. N. Sudhan, K. Subramani, M. Karnan, N. Ilayaraja and M. Sathish, *Energy Fuels*, 31 (2017) 977.
14. H. Feng, H. Hu, H. Dong, Y. Xiao, Y. Cai, B. Lei, Y. Liu and M. Zheng, *J. Power Sources*, 302 (2016) 164.
15. X. Han, K. Tao, D. Wang and L. Han, *Nanoscale*, 10 (2018) 2735.
16. C. Qu, L. Zhang, W. Meng, Z. Liang, B. Zhu, D. Dang, S. Dai, B. Zhao, H. Tabassum, S. Gao, H. Zhang, W. Guo, R. Zhao, X. Huang, M. Liu and R. Zou, *J. Mat. Chem. A*, 6 (2018) 4003.
17. A. Afzal, F. A. Abuilaiwi, A. Habib, M. Awais, S. B. Waje and M. A. Atieh, *J. Power Sources*, 352 (2017) 174.
18. Q. Meng, K. Cai, Y. Chen and L. Chen, *Nano Energy*, 36 (2017) 268.
19. D. D. Guo, R. R. Xin, Y. F. Wang, W. Jiang, Q. P. Gao, G. S. Hu and M. H. Fan, *Microporous Mesoporous Mat.*, 279 (2019) 323.
20. G. P. Awasthi, D. P. Bhattarai, B. Maharjan, K. S. Kim, C. H. Park and C. S. Kim, *J. Indust. Eng. Chem.*, 72 (2019) 265.
21. A. Jain, R. Balasubramanian and M. P. Srinivasan, *Chem. Eng. J.* 283 (2016) 789.
22. Y. Zhang, S. Liu, X. Zheng, X. Wang, Y. Xu, H. Tang, F. Kang, Q.-H. Yang and J. Luo, *Adv. Funct. Mat.*, 27 (2017) 1604687.
23. G. Zhao, C. Chen, D. Yu, L. Sun, C. Yang, H. Zhang, Y. Sun, F. Besenbacher and M. Yu, *Nano Energy*, 47 (2018) 547.
24. Y.-Q. Zhao, M. Lu, P.-Y. Tao, Y.-J. Zhang, X.-T. Gong, Z. Yang, G.-Q. Zhang and H.-L. Li, *J. Power Sources*, 307 (2016) 391.
25. W. Qian, F. Sun, Y. Xu, L. Qiu, C. Liu, S. Wang and F. Yan, *Energy Environ. Sci.*, 7 (2014) 379.
26. Y. Han, N. Shen, S. Zhang, D. Li and X. Li, *J. Alloys Compd.*, 694 (2017) 636.
27. F. Ma, S. L. Ding, H. J. Ren and Y. H. Liu, *RSC Adv.*, 9 (2019) 2474.
28. K. Wang, N. Zhao, S. Lei, R. Yan, X. Tian, J. Wang, Y. Song, D. Xu, Q. Guo and L. Liu, *Electrochim. Acta*, 166 (2015) 1.
29. M. Sivachidambaram, J. J. Vijaya, K. Niketha, L. J. Kennedy, E. Elanthamilan and J. P. Merlin, *J. Nanosci. Nanotechnol.*, 19 (2019) 3388.
30. Y. J. Li, G. L. Wang, T. Wei, Z. J. Fan and P. Yan, *Nano Energy*, 19 (2016) 165.
31. Z. Li, W. Lv, C. Zhang, B. Li, F. Kang and Q.-H. Yang, *Carbon*, 92 (2015) 11.
32. B. Liu, Y. Liu, H. Chen, M. Yang and H. Li, *J. Power Sources*, 341, (2017) 309.
33. B. Zhu, B. Liu, C. Qu, H. Zhang, W. Guo, Z. Liang, F. Chen and R. Zou, *J. Mat. Chem. A*, 6

- (2018) 1523.
34. L. Shi, L. Jin, Z. Meng, Y. Sun, C. Li and Y. Shen, *RSC Adv.*, 8 (2018) 39937.
 35. C. Wang, Y. Xiong, H. Wang and Q. Sun, *J. Colloid Interface Sci.* 528 (2018) 349.
 36. C. Xuan, Z. Peng, J. Wang, W. Lei, K. Xia, Z. Wu, W. Xiao and D. Wang, *Chinese Chem. Lett.*, 28 (2017) 2227.
 37. W. Zhang, J. Xu, D. Hou, J. Yin, D. Liu, Y. He and H. Lin, *J. Colloid Interface Sci.*, 530 (2018) 338.
 38. Z. Fan, Q. Zhao, T. Li, J. Yan, Y. Ren, J. Feng and T. Wei, *Carbon*, 50 (2012) 1699.
 39. C. C. Xu, F. Xu, L. X. Sun, L. Z. Cao, F. Yu, H. Z. Zhang, E. H. Yan, H. L. Peng, H. L. Chu and Y. J. Zou, *Int. J. Electrochem. Sci.*, 14(2019) 1782.
 40. Y. Deng, Y. Ji, H. Wu and F. Chen, *Chem. Comm.*, 55 (2019) 1486.
 41. Y. Zhou, J. Ren, Y. Yang, Q. Zheng, J. Liao, F. Xie, W. Jie and D. Lin, *J. Solid State Chem.*, 268 (2018) 149.

© 2019 The Authors. Published by ESG (www.electrochemsci.org). This article is an open access article distributed under the terms and conditions of the Creative Commons Attribution license (<http://creativecommons.org/licenses/by/4.0/>).